

# **Aquarius Scatterometer Calibration**

*AQ-014-PS-0017*

ALEXANDER G. FORE, GREGORY NEUMANN, ADAM P. FREED-  
MAN, MARIO J. CHAUBELL, WENQING TANG, AKIKO K. HAYASHI,  
AND SIMON H. YUEH

**Abstract**—In this paper we discuss the Aquarius scatterometer calibration, starting with the instrument calibration. We examine the stability of Aquarius as quantified using the loop-back power and estimated receiver gain to shown Aquarius has been extremely stable to order 0.1 dB since mission start. We show the temperatures of scatterometer components not contained in the loop-back path have been controlled precisely to  $0.5^\circ\text{C}$  to minimize any temperature dependent losses. Combined, these results show Aquarius produces accurate  $\sigma_0$  over the mission lifetime. In the next section we discuss the stability as quantified using external models and again show stability to order 0.1 dB in very good agreement with instrument-only methods. Then we discuss the methods used to absolutely calibrate Aquarius  $\sigma_0$  with respect to previous L-band radar systems. We show that Aquarius is relatively calibrated to order 0.1 dB for co-polarization channels and better than 0.2 dB for cross-polarization channels. Finally we discuss the calibration of the Aquarius wind speed product. We compare the Aquarius wind speed with radiometer wind speed products, other radar scatterometers, and numerical weather products. We show that the Aquarius instrument provides a wind speed product similar but slightly worse than traditional pencil-beam scatterometers.

## I. INTRODUCTION

Aquarius is a combined active / passive L-band microwave instrument developed to map the salinity field at the surface of the ocean from space [1], [2]. The primary science objective of this mission is to monitor the seasonal and inter-annual variation of the large scale features of the sea surface salinity (SSS) field in the open ocean with a spatial resolution of 150 km and a retrieval accuracy of 0.2 practical salinity units (psu) globally on a monthly basis. The measurement principle is based on the response of L-band (1.413 GHz) sea surface brightness temperature ( $T_B$ ) to SSS. However, the ocean surface roughness effect on  $T_B$  is larger than that due to SSS so estimation of the excess emissivity due to sea surface roughness is critical to achieve the required accuracy. To this end, Aquarius includes a scatterometer to help correct for this surface roughness effect.

The Aquarius instrument has three antenna beams operating at about  $29^\circ$ ,  $38^\circ$ , and  $46^\circ$  incidence angle [1]. Each antenna beam has one radiometer (1.413 GHz), which can acquire the first three Stokes parameters of microwave radiation. The three antenna beams operate in a push-broom mode that maps a swath 390 km wide and covers the globe once every 7 days. The radiometer antenna feeds are shared with one scatterometer (1.26 GHz), that cycles through the three feeds and acquires the normalized radar cross section ( $\sigma_0$ ) for co- and cross-polarization. The cycling between radiometer and scatterometer is done quickly enough so that we average them into observations that are essentially collocated in space and time in the level 2 data product. There are two baseline products from the Aquarius scatterometer: radar  $\sigma_0$  and ocean surface wind speed. The radar  $\sigma_0$  product is radiometrically calibrated and geolocated. The primary geophysical product estimated from the Aquarius scatterometer is the surface wind speed. Typically the backscatter of the ocean is modeled to be a function of both surface wind speed and the wind direction relative to the radar look direction, however, due to the push-broom sampling of Aquarius we only obtain one azimuthal look at the ocean surface. Thus we are unable to determine

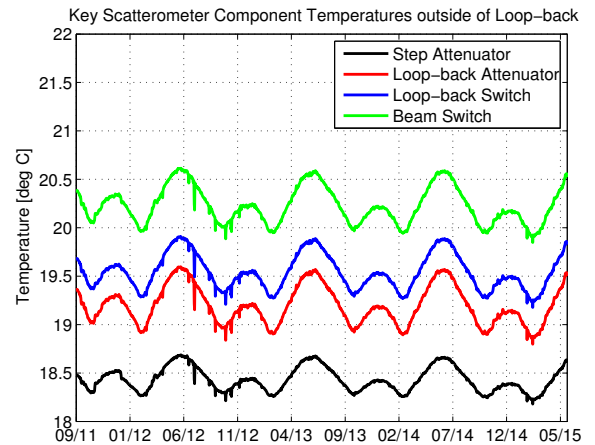


Fig. 1. Step attenuator (black), loop-back attenuator (red), loop-back switch (blue), and beam switch (green) temperatures. All of these components are outside of the loop-back path and are under active thermal control to minimize any variation in losses of these parts as a function of temperature. We see less than  $0.5^\circ\text{C}$  variations over the mission duration.

the surface wind speed and direction separately. Calibrated surface wind speeds are essential to the sea surface salinity algorithm, as the surface roughness contribution to emissivity is very significant compared to the salinity contribution to emissivity.

In Section II we discuss the thermal environment and instrument-only calibration of the radar. In Section III we use the ocean as a reference target to further study the radar calibration and track changes over time. In Section IV we examine the absolute calibration of Aquarius as compared to other L-band radars. Finally in Section V we assess the performance of the Aquarius wind speed product.

## II. RADAR ENGINEERING PARAMETERS

### A. Temperatures

The fundamental goal of the Aquarius scatterometer is the accurate measurement of  $\sigma_0$ , which is essential to the estimate of ocean surface wind speed – the key science product of the Aquarius scatterometer. Other science parameters are derived from this measurement and accuracy must be maintained over the entire mission duration. A key tool to ensure the calibration stability of any radar system is a loop-back calibration feature where a portion of the transmit power is fed through an attenuation path and back into the receiver. Thus, as long as this attenuation path is stable, and with appropriate ground processing, any electronics drift due to temperature or aging of components behind this loop-back point is automatically cancelled in the calculation of  $\sigma_0$ . The accuracy of  $\sigma_0$  also depends on the stability of components and interconnections beyond the point of the loop-back path. In particular, temperature variations can cause changes in losses of radar electronic components and interconnections not in the loop-back path. For this reason, Aquarius was designed to minimize these changes by maintaining a constant temperature for these critical components using automatic temperature control. Data shows that the temperature of sensitive components within the

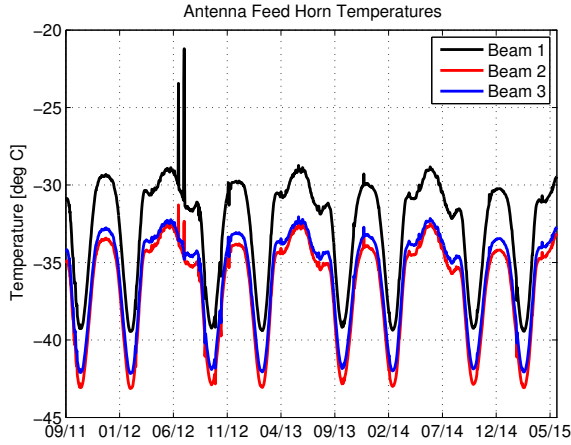


Fig. 2. Antenna feed-horn temperatures (beam 1 - black, 2 - red, 3 - blue). These are not under thermal control and show order  $10^{\circ}$  C variations over the mission duration. It is difficult to control the temperature of the feed-horn assembly, since it is exposed to the environment. The feed assembly is protected by a sun-shade, which minimizes temperature changes. The effects on  $\sigma_0$  are verified by analysis.

scatterometer and outside of the loop-back path have been controlled to better than  $1^{\circ}$  C over the entire mission as shown in Figure 1. In this figure we plot the temperatures on various key attenuators and switches under active thermal control and we show the temperatures are maintained to less than  $0.5^{\circ}$  C variations over the mission. Every effort is made to use only the highest quality components and interconnects, however, holding the temperature nearly constant removes one of the error contributors for components of this type.

Other components which were more difficult to control, such as the feed and antenna, were designed to be insensitive to changing temperatures so as to not introduce additional temperature-dependent losses into the  $\sigma_0$ . For example, a sun shade was incorporated to minimize temperature changes on the feed. We examine the temperatures on the feed and antenna reflector assembly as these temperatures are not under active thermal control. In Figure 2 we plot the temperatures on the antenna beam feed-horns which show some variations with time, as large as  $10$  to  $15^{\circ}$  C over the duration of the mission. The daily average is slowly varying over the seasons, while the feed temperature changes by several degrees over an orbit. These variations in feed horn temperature are expected and do not induce a significant variation in the calibration. Additionally any sharp temperatures changes on these plots are due to periods when the spacecraft attitude is not controlled or in a nominal state, such as during a cold sky maneuver.

### B. Transmit Power / Receiver Gain

In Figure 3 we plot the loop-back power as a function of time and we observe the most change at the beginning of the mission. We only show the loop-back powers for beam 1, those for beams 2 and 3 are extremely similar and show the same drifts and variations as for beam 1. The radiometer correlated noise diode (CND), though part of the radiometer, can be used to estimate the scatterometer receiver gain. The

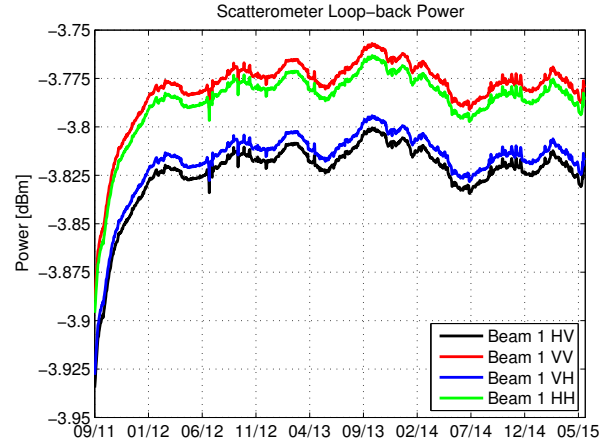


Fig. 3. Scatterometer loop-back power as a function of time for the four polarizations on Beam 1. The various loop-back powers for beams 2 and 3 are similar and we omit them for clarity. Note that changes in loop-back as a function of time do not reflect an error in  $\sigma_0$  as they are automatically removed in ground processing.

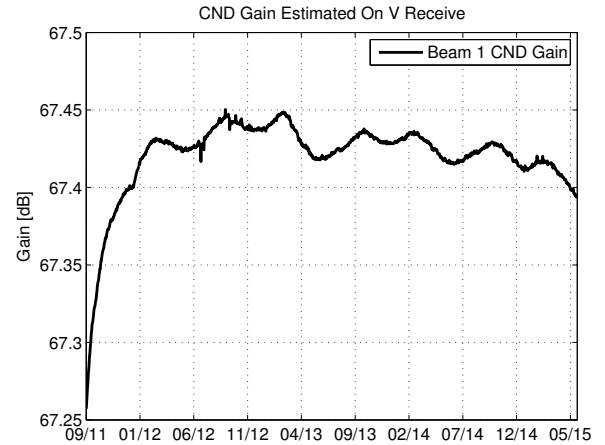


Fig. 4. Scatterometer gain estimated using adjacent noise-only observations with and without the CND firing for beam 1. Again we omit beams 2 and 3 for clarity as they are very similar to beam 1. Note the scatterometer gain estimated by the CND ratio increases by about  $0.2$  dB over the first few months.

CND is used for the radiometer calibration and fires into every other noise-only scatterometer observation. Using the known CND power and adjacent noise-only observations we may estimate the scatterometer receiver gain. The receiver gain estimate is given by the difference in the noise powers observed with the CND firing and without divided by the known CND power. The magnitude of the change seen over the first year is similar to the change in the scatterometer loop-back calibration, indicating that a portion of the change observed by the loop-back calibration measurement was due to a change in the receiver gain. In Figure 4 we plot the gain obtained using this method as a function of time, again observing a drift in the initial few months and stability ever since. Again we only show the CND estimated receiver gain for beam 1 – those obtained for beams 2 and 3 are very similar.

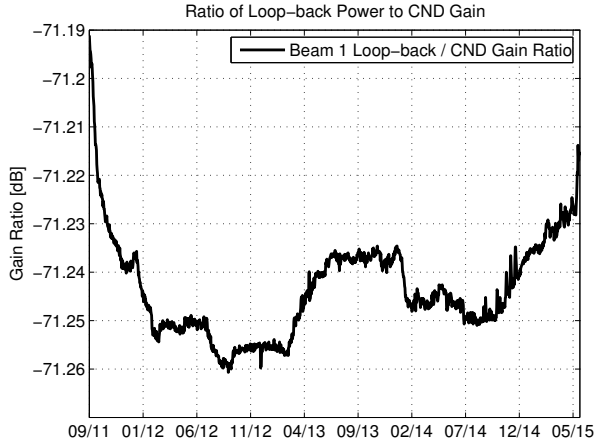


Fig. 5. Ratio of loop-back power to CND estimated scatterometer gain for beam 1. We omit beams 2 and 3 for clarity as they are very similar. Note that the CND gain has a larger initial increase than the loop-back power, as we can see here by the 0.07 dB decrease in this ratio.

As the trends in Figures 3 and 4 are not the same, there is a part of the change in the loop-back power that is not due to any observed change in the scatterometer gain estimated by the CND. In Figure 5 we plot the ratio of the loop-back power to the CND gain for beam 1 to determine the magnitude of this difference. The loop-back power to CND gain ratios for beams 2 and 3 are also extremely similar and we omit them for clarity. These differences may be due to any combination of the following reasons: changes in transmit power, changes in CND power output, and changes in losses in cabling between the CND and the loop-back path. If it is due to transmit power or CND output it will have no effect on the accuracy of  $\sigma_0$ , however, if we assume that the observed change is all due to changes in interconnect loss it would cause a maximal drift in  $\sigma_0$  of 0.14 dB, double the observed change in the ratio as the signal passes through this cable twice. Taken together these plots show that the Aquarius instrument produces radiometrically stable  $\sigma_0$  over the life of the mission.

### III. RADAR MEASURED $\sigma_0$ - EXPECTED $\sigma_0$

Next we compare the observed radar  $\sigma_0$  to the expected  $\sigma_0$  ( $\sigma_0^{exp}$ ) which is that predicted by an ancillary numerical weather product (NWP), in this case from the National Centers for Environmental Prediction (NCEP), coupled with the geophysical model function (GMF) discussed in Section V-B. The  $\sigma_0^{exp}$  contained in the Aquarius level 2 data products is used in this analysis. We introduce  $\Delta\sigma_0 := \sigma_0 - \sigma_0^{exp}$  as this difference. Tracking the variations in  $\Delta\sigma_0$  allow an independent assessment of any possible drifts in the scatterometer calibration over time or with geographic location which we then compare to the assessments performed in Section II.

#### A. $\Delta\sigma_0$ as a Function of Time

First we perform averages of the  $\Delta\sigma_0$  conditioned on time to track residual changes in  $\sigma_0$  after accounting for the expected changes in  $\sigma_0$  due to changes tracked by the NCEP wind

speed. In Figure 6 we plot this quantity as a function of time for the mission duration. We observe an initial transient change which dies out over the course of the first few months of the mission. We also see that the drift and subsequent wiggles are highly correlated across the three antenna beams and polarizations, indicating the underlying cause is in the shared portion of the three antenna beams. The observed drift of about 0.13 dB in Figure 6 is consistent with the picture we present in Section II-B where we estimate a worst-case drift of 0.14 dB if we assume CND power and transmit power are stable. In versions 4.0 and higher of the Aquarius data this initial transient drift in calibration as a function of time was removed using an exponential fit.

#### B. $\Delta\sigma_0$ as a Function of Location

In Figure 7 we show maps of the averaged  $\Delta\sigma_0$  for the entire mission duration for all three beams. We collocate the Aquarius data with SSMI/S as described in Section V-A and only consider data where SSMI/S indicates no rain, then bin onto a  $1^\circ \times 1^\circ$  map. We only see significant differences in the equatorial rain bands and at high latitudes. Even though we collocate with SSMI/S to remove rain we may still have residual rain effects in the  $\Delta\sigma_0$  coming in due to errors in the NWP model and / or the inability of the NWP model to resolve rain. Similarly, at high latitudes the NWP model may not capture the higher wind speeds generally observed by scatterometers.

## IV. RADIOMETRIC CALIBRATION

Next we consider the overall average radiometric calibration of Aquarius with respect to previous L-band radar systems such as PALSAR and JERS-1.

#### A. Land Calibration

Over land we consider the Amazon rainforest as a calibration site, giving estimates of the absolute calibration as well as calibration stability over time. The Amazon rainforest has a long heritage of use as a calibration target for L-band radar systems such as Japan Earth Resources Satellite 1 (JERS-1) [3] and Phased Array type L-band Synthetic Aperture Radar (PALSAR) [4]. These papers show that the Amazon  $\gamma_0$ , where  $\gamma_0 := \sigma_0 / \cos(\theta_i)$  and  $\theta_i$  is the incidence angle, is independent of  $\theta_i$  over a wide range of  $\theta_i$ , with  $-6.28$  dB for HH polarization,  $-11.25$  dB for HV polarization, and that the wet season  $\gamma_0$  is larger than the dry season  $\gamma_0$  by 0.27 dB.

The scattering from this region of the Amazon rainforest is dominated by the canopy which is randomly oriented and we expect the HH and VV polarization back-scatter to be similar (see [5] for example). In Figure 8 we show a color-composite image of the Amazon rainforest at L-band from PALSAR. We use the HH  $\sigma_0$  for the red and blue channels while the HV  $\sigma_0$  is used for the green. This allows us to separate volume and surface scattering easily as volume scattering shows up as green whereas surface scattering is purple to nearly black depending on surface roughness. We choose the region inside the blue polygon that is not also contained in the black

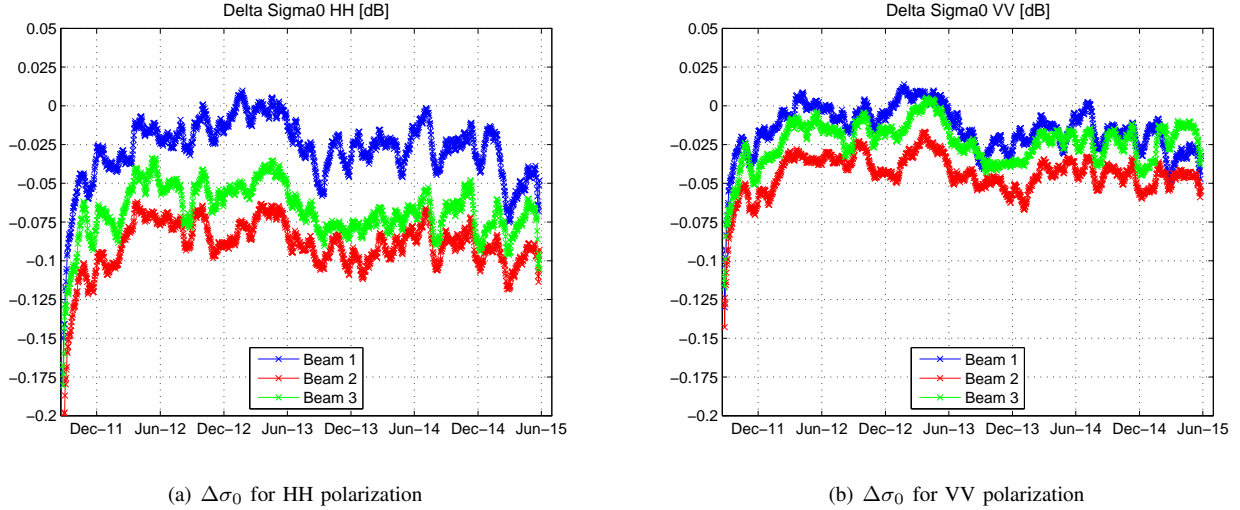


Fig. 6. (a)  $\Delta\sigma_0$  computed using HH polarization, and (b)  $\Delta\sigma_0$  computed using VV polarization. In each we plot Beam 1 (blue), Beam 2 (red), and beam 3 (green). Note the initial transient drift of order 0.1 dB in measured  $\sigma_0$  as compared to  $\sigma_0^{exp}$  over the first few months of Aquarius mission.

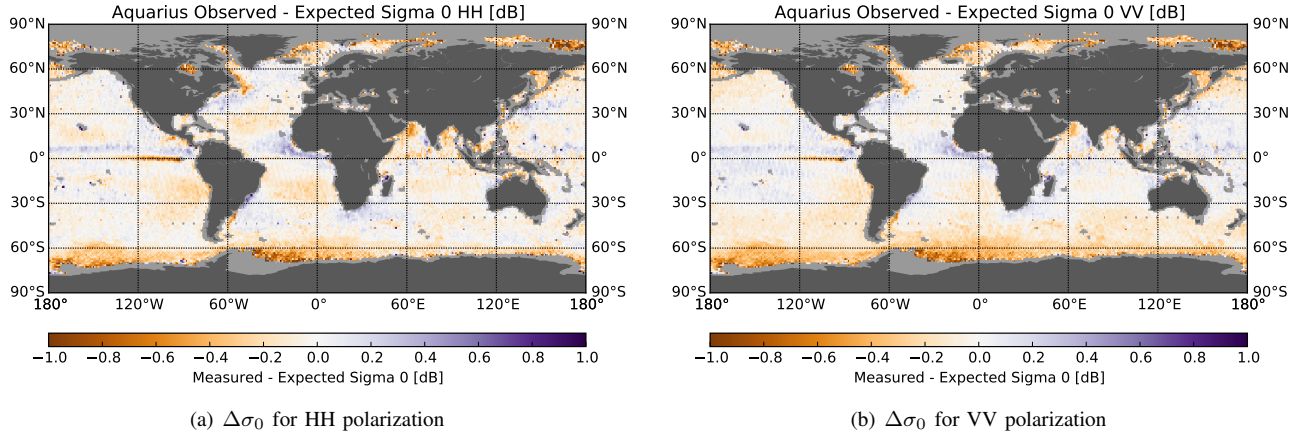


Fig. 7. (a) Map of  $\Delta\sigma_0$  computed using HH polarization, and (b) the same for VV polarization. In each we average all three beams together for the entire mission duration to date. We see that generally there is not a geographic correlation of the differences in measured and expected  $\sigma_0$ , with the exception of the equatorial rain bands and high wind speeds at high latitudes.

polygon as the calibration region. This region was selected as it contains a large region, as compared to beam footprint, of nearly homogenous volume back-scatter, without rivers or other non-forest features, with the exception of the smaller black polygon. PALSAR and JERS-1 have selected different region (see Figure 1 of [4] for PALSAR and Figure 1 of [3] for JERS-1), however, that region is not large enough for Aquarius to sample with all three beams.

We extract all Aquarius observations within this region and compute the overall average value. In Table I we summarize the overall biases as compared to the PALSAR results discussed in [4]. We average over 3 full yearly seasonal cycles in the Aquarius data to ensure we do not bias the result towards the wet or dry season. We find that co-polarization channels are calibrated to about the 0.1 dB level as compared to PALSAR while the cross-polarization channels are at the 0.2 dB level, and that there is no significant ascending / descending difference. While each beam and ascending / descending combination are not exactly the same we do not consider the

TABLE I  
SUMMARY OF AQUARIUS AMAZON  $\gamma_0$  BIASES WITH PALSAR

	Beam 1	Beam 2	Beam 3
All HH	0.02	0.08	0.12
Ascending HH	0.04	0.07	0.06
Descending HH	-0.01	0.09	0.20
All VV	-0.04	0.06	0.07
Ascending VV	-0.02	0.04	0.06
Descending VV	-0.05	0.07	0.09
All HV	0.06	0.21	0.13
Ascending HV	0.08	0.19	0.09
Descending HV	0.05	0.22	0.19

differences to be significant.

We observe an annual variation in the Amazon  $\gamma_0$  as shown in Figure 9. The wet season in the Amazon runs from November to May where we observe a steady increase in  $\sigma_0$  of

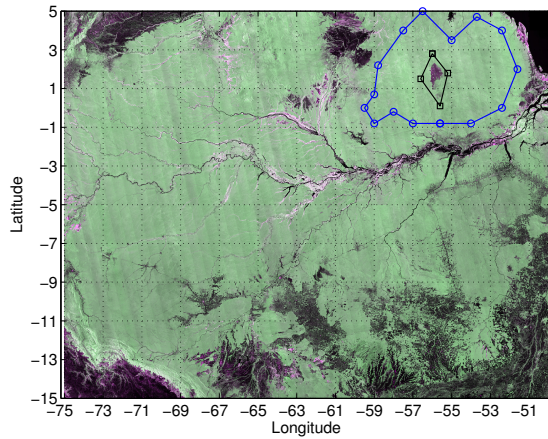


Fig. 8. Color-composite image of Amazon at L-band where HH is shown as red and blue while HV is green. Regions with strong volume scattering appear green while those with surface scattering appear purple. We use all Aquarius footprints falling within the blue polygon that are not also within the black polygon for analysis.

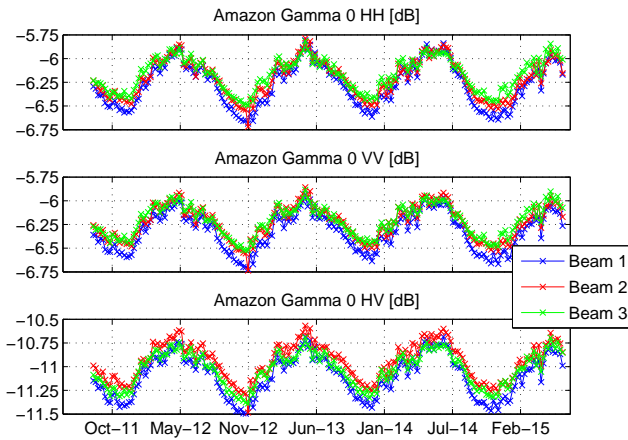


Fig. 9. Aquarius Amazon  $\gamma_0$  as a function of time for the entire Aquarius mission. We see an order 0.5 dB seasonal cycle and a very high level of repeatability in the time series between years as well as between beams and channels.

about 0.5 dB over those six months. In the dry season we see a decrease in  $\sigma_0$  of the same size. This wet-dry seasonal cycle is very stable over the three years of Aquarius observations, in all polarizations and beams. The peak-to-peak seasonal variation in Aquarius is significantly larger than reported for JERS-1, however, it is not clear how much data was used to generate that figure for JERS-1. Additionally, the footprint size of Aquarius necessitates the use of a different region of the Amazon than JERS-1, which may have differing amounts of total rainfall accumulation in the two regions.

### B. Ocean Calibration

In [6] a GMF for PALSAR HH polarization was derived by collocation with Advanced Scatterometer (ASCAT). This GMF covers a wide range of incidence angles so it provides a useful point from cross-comparison of Aquarius to other L-

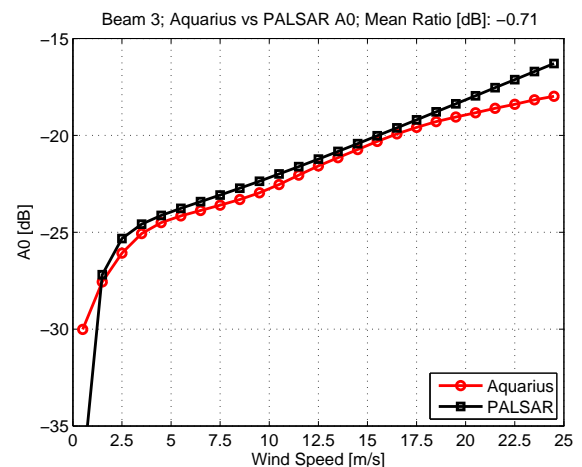
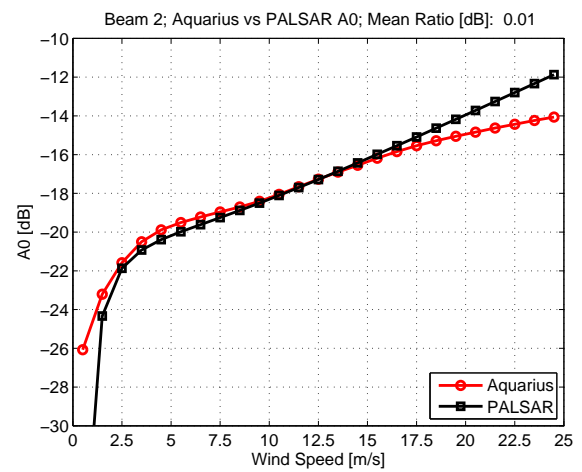
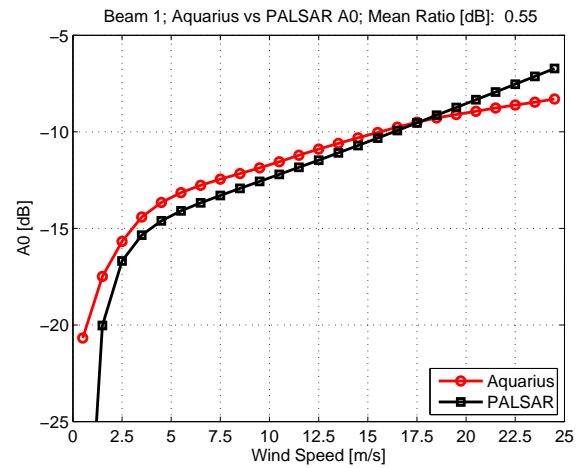


Fig. 10. Aquarius and PALSAR A0 (non-directional part of GMF) for HH polarization versus wind speed for beam 1 (top), 2 (middle), and 3 (bottom). In each plot the title shows the average ratio, weighted by the overall ocean with speed distribution. We find that the Aquarius model function and the PALSAR model function are in agreement to better than 1 dB for all beams.

band sensors. In Figure 10 we plot the non-directional portion of the HH GMF for both Aquarius and the PALSAR GMF evaluated at the Aquarius incidence angles as a function of wind speed for the three Aquarius beams. We observe that the model functions are very similar in shape up to about 17 m/s wind speed. Above this point statistics are generally very poor and differences in the reference wind speed used to train each GMF may dominate the difference. We also compute the overall wind speed distribution weighted mean difference between the two GMFs in the title, and we find 0.55 dB for beam 1, 0.01 dB for beam 2, and  $-0.71$  dB for beam 3. Overall the agreement is reasonably good, especially considering that the Aquarius GMF is trained against Special Sensor Microwave Imager (SSM/I/S) winds while that for ASCAT is trained against European Centre for Medium-Range Weather Forecasts (ECMWF).

### V. AQUARIUS SCATTEROMETER WIND SPEED PERFORMANCE

We have shown that the Aquarius scatterometer has provided accurate  $\sigma_0$  over the life of the mission. Wind speed is the fundamental geophysical product of the Aquarius scatterometer, giving the surface roughness corrections needed for accurate salinity processing. The relationship between ocean surface wind speed and scatterometer  $\sigma_0$  has been studied in detail for other wavelengths (Ku and C in particular), however, Aquarius is the first L-band scatterometer. In [12] the relationship between Aquarius  $\sigma_0$  and wind speed is derived, and we find it varies from  $-22$  dB to  $-18$  dB for wind speeds between 5 to 15 m/s, giving a sensitivity of approx. 0.4 dB in  $\sigma_0$  per m/s wind speed. As the relationship between  $\sigma_0$  and wind speed is non-linear, a calibrated  $\sigma_0$  input does not ensure a calibrated, or calibrate-able, wind speed output. Hence we undertake the wind speed calibration study in this section to show that the wind speed algorithm is generating calibrated output wind speed products.

In [7] we have previously introduced and validated the Aquarius scatterometer-only wind speed products. Here we revisit this analysis of the Aquarius scatterometer wind speed using significantly more data and the Aquarius version 3.0 data products. We do not consider buoy validations due to a large mis-match in spatial sampling between the order 100 km footprints of Aquarius and the point observations of buoys. Instead we consider various other wind products: RapidScat, SSM/I/S, and WindSAT which have all been inter-calibrated with each other [8], [9]. These papers discuss the calibration / validation of the QuikSCAT wind processing and model function used for Ku-band scatterometers. RapidScat continues the heritage of inter-calibrated Ku-band scatterometers as it has been cross-calibrated with QuikSCAT.

#### A. Datasets

We generate a set of collocations that include wind speed and rain rate from version 7<sup>1</sup> SSM/I/S data [10] and operational wind data from ECMWF. Every SSM/I/S data point

<sup>1</sup>SSM/I/S data are produced by Remote Sensing Systems and sponsored by the NASA Earth Science MEaSUREs DISCOVER Project. Data are available at [www.remss.com](http://www.remss.com)

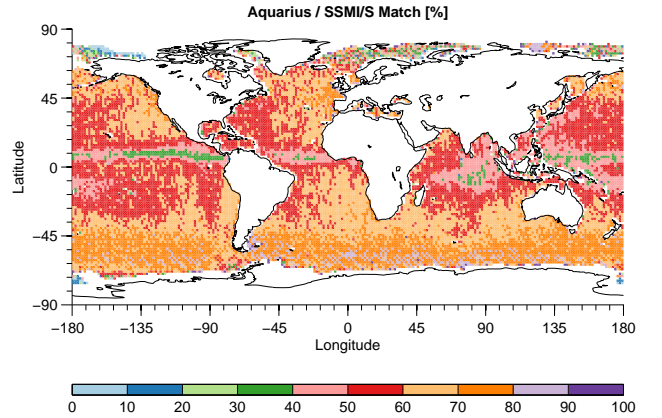


Fig. 11. Percent of Aquarius data for which there is a rain-free SSM/I/S matchup. More than 50% of Aquarius footprints have a suitable matchup with SSM/I/S except for regions having significant rain in a narrow equatorial band.

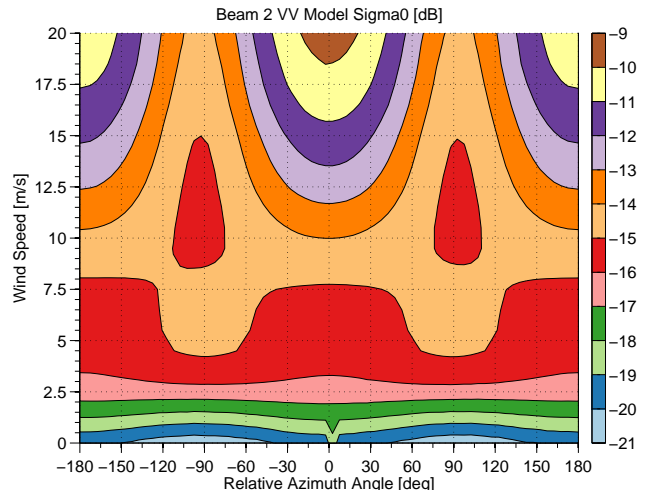


Fig. 12. Aquarius model backscatter as a function of wind speed and relative azimuth angle for Beam 2 VV polarization. Note the closed contours indicating a local maxima and non-monotonic relationship between  $\sigma_0$  and wind speed at crosswind relative azimuth angles. Also note the change in sign of  $A_2$  at about 7.5 m/s and the small directional signal below 10 m/s.

within 28 km in space and one hour in time are averaged into one collocation data point. Furthermore, we require that scatterometer quality flag bits 31, 29, 21, and 20 are not set, indicating lack of severe radio frequency interference and no pointing errors. Finally we only consider data within  $\pm 50^\circ$  latitude to remove residual ice contamination. We obtain a dataset containing more than 40 million data points due to the very good overlap between SSM/I/S F17 and Aquarius. In Figure 11 we show the overall spatial distribution of the Aquarius footprints which have a rain-free SSM/I/S matchup. We see that the match-ups are evenly distributed, with the expected reduction in rain-free match-ups due to the equatorial rain band.

#### B. Geophysical Model Function

As Aquarius is the first L-band scatterometer, it provides great insight into the radar model function which relates the

TABLE II  
AQUARIUS-SSMI/S-ECMWF GLOBAL COLLOCATION WIND SPEED MEAN  
AND STANDARD DEVIATION.

	Speed Mean [m/s]	Speed STD [m/s]
SCAT	7.4667	3.4347
SSMI/S	7.4840	3.2716
ECMWF	7.4611	3.1785

observed backscatter to the ocean surface wind speed and wind direction. Previous estimates of L-band model functions were based on synthetic aperture radar (SAR) [6] or aircraft data [11]. The full description of our L-band model functions is developed in [12], however we will provide a brief idea of the method here. We derive the Aquarius model function for L-band using SSMI/S as the reference wind speed and the NCEP wind direction. Next we bin the data into wind speed bins and for each bin we perform a least-squares fit of the observed backscatter to a two-term cosine fit of the form

$$\sigma_0^m(w, \phi) = A_0(w) + A_1(w) \cos \phi + A_2(w) \cos(2\phi),$$

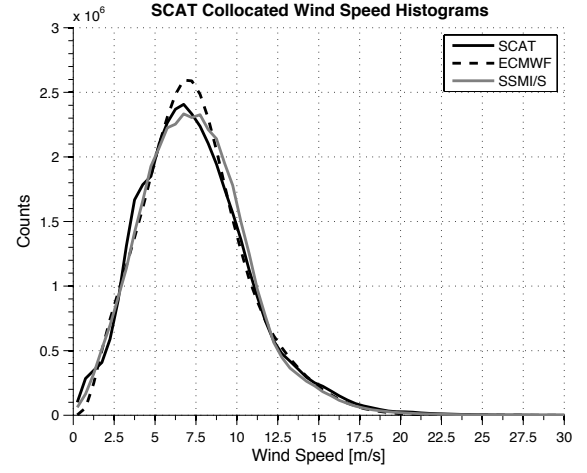
where  $w$  is the wind speed and  $\phi$  is the NCEP wind direction relative to the radar azimuth angle. Finally we perform some smoothing for higher wind speeds and extrapolation to extreme wind speeds.

Next we emphasize some peculiar features of the ocean  $\sigma_0$  at L-band relevant to the scatterometer wind speed retrieval. Previous experience with Ku and C-band scatterometers has generally proven that  $\sigma_0$  is monotonically related to the wind speed at all azimuth angles. In Figure 12 we show a contour plot of the model  $\sigma_0$ , as a function of wind speed (vertical axis) and relative azimuth angle (horizontal axis) for Aquarius beam 2, VV polarization. For cross-wind relative azimuth angles, near  $\pm 90^\circ$ , we observe a non-monotonic relationship between wind speed and radar  $\sigma_0$ , clearly indicated by the closed contour line. In addition there is a change in sign of the  $A_2$  term near 8 m/s where below this level crosswind has higher  $\sigma_0$  than upwind and downwind while above this level crosswind has lesser  $\sigma_0$  than upwind and downwind. This change in sign also causes the model function to have little azimuthal dependance near the peak of the global wind speed distribution near 7.5 m/s.

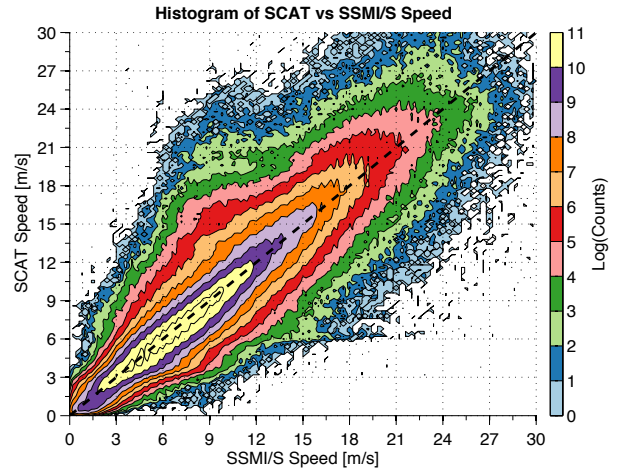
### C. Aquarius Speed versus ECMWF and SSMI/S

In Figure 13 we show the one dimensional histograms of Aquarius wind speed, ECMWF wind speed, and SSMI/S wind speed as well as the joint distribution of Aquarius wind speed and SSMI/S wind speeds. We note that all three wind speed products have a similar shape in 13(a), and that the majority of the data is centered around the 1:1 line in 13(b). In Table II we show the means and standard deviations (STD) of each of the three wind speeds and observe that all three are very consistent.

Next we compute the conditional Aquarius wind speed bias and standard deviation as a function of SSMI/S wind speed in Figure 14. We observe nearly zero speed bias until SSMI/S speed is greater than 20 m/s. The overall standard deviation



(a) Wind Speed Histograms



(b) Joint Histograms

Fig. 13. (a) Histograms of Aquarius wind speed (solid black line), ECMWF wind speed (dashed black line), and SSMI/S wind speed (grey line). (b) Joint log-histogram of SSMI/S wind speed (horizontal axis) and Aquarius wind speed (vertical axis). The Aquarius / SSMI/S joint histogram shows the Aquarius and SSMI/S data are in very good agreement with the vast majority centered about the 1:1 line.

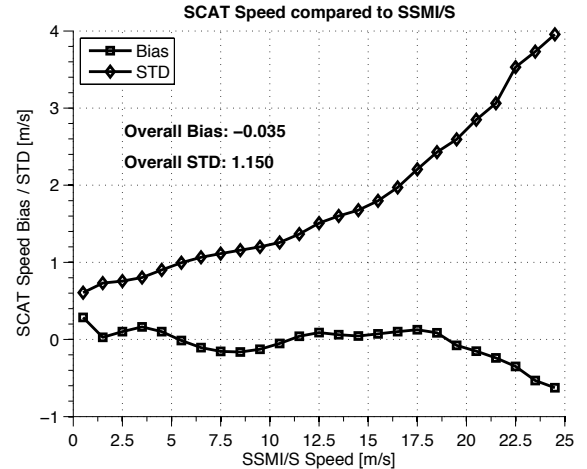


Fig. 14. Conditional Aquarius - SSMI/S mean speed difference (squares) and standard deviation (diamonds) as a function of SSMI/S wind speed. The overall mean speed difference is  $-0.035$  m/s and STD is 1.150 m/s.

TABLE III  
AQUARIUS SCATTEROMETER WIND SPEED TRIPLE-COLLOCATION  
RESULTS

	SSMI/S	ECMWF	Aquarius
Bias [m/s]	0	0.2730	-0.1184
Slope	1	0.9480	1.0181
Error [m/s]	0.6668	0.7925	0.9394
	SSMI/S	RapidScat	Aquarius
Bias [m/s]	0	0.3762	-0.1150
Slope	1	0.9655	1.0176
Error [m/s]	0.6636	0.6844	0.9417

of the difference is 1.15 m/s, on par with other scatterometers [9].

#### D. Triple-Collocation

Finally we use the triple-collocation methods presented in [13], [14] to determine the partition of the error between Aquarius, SSMI/S, and other wind speed products. Triple-collocation analysis allows us to separately estimate the variances for each of the three wind speeds that are collocated together, subject to some assumptions. The assumptions are that the wind speed errors on each are uncorrelated and that they are zero-mean. In [7] we give the derivation of the triple-collocation analysis used here, so we refer the reader to that paper for more detail. We perform two triple-collocation analyses: the first using Aquarius, SSMI/S, and ECMWF while the second uses RapidScat instead of ECMWF. Both analyses are presented in Table III. The results of the triple-collocation analysis using Aquarius, SSMI/S, and ECMWF show that the Aquarius error is about 0.94 m/s, the SSMI/S error is 0.67 m/s, and that for ECMWF is 0.79 m/s. The errors presented here are the square-root of the variance determined using the triple-collocation analysis.

RapidScat is a Ku-band scatterometer on the International Space Station, assembled with heritage QuikSCAT / SeaWinds hardware. The version 1.0 climate 12.5 km wind products have been released on the Physical Oceanography Distributed Active Archive Center (PODAAC) and we use them for this study. Previously in [7] we performed a triple-collocation analysis with QuikSCAT, however that only used one week of data, whereas with RapidScat we use six months of data. For every Aquarius footprint we average all rain-free RapidScat wind vector cells that lie within 25 km in space into one collocation data point. For the analysis presented here we then only consider collocated data points that are within 30 minutes in time and with latitudes between  $\pm 45^\circ$ . Due to the RapidScat orbit a great number of the match-ups are around  $\pm 50^\circ$  latitudes and we attempt to obtain a less exaggerated sampling by excluding these regions. In Table III we present the results of the triple-collocation analysis with RapidScat. We find that the Aquarius random error component is 0.94 m/s, while that for SSMI/S is 0.66 m/s, and RapidScat is 0.68 m/s. The two analysis suggest that the Aquarius wind speed product has an accuracy that is better than 1.00 m/s.

## VI. CONCLUSION

We have examined the calibration of the Aquarius scatterometer in multiple ways. The loop-back calibration feature ensures automatic calibration for a large portion of the Aquarius scatterometer instrument. We have shown that key components of the scatterometer not contained in the loop-back pathway have excellent thermal control, with thermal stability to  $0.5^\circ$  C, minimizing possible temperature dependent losses of these components. By examining the look-back and estimated CND gain we constrain any calibration drift in Aquarius backscatter over the mission to order 0.1 dB. By comparing Aquarius backscatter with an ancillary ocean model we provide further support of this key calibration level, where we have observed 0.13 dB drift in measured backscatter as compared to expected backscatter over the mission duration. This observed drift is consistent with the instrument-only analysis. Combined these results prove that Aquarius provides a temporally stable source of L-band  $\sigma_0$  for the mission duration.

Next we study the Amazon rain forest to compare the calibration of Aquarius to other L-band radar systems and find the Aquarius co-polarizations are calibrated at the 0.1 dB level and cross-polarizations at 0.2 dB. Then we compared the Aquarius GMF to the PALSAR GMF as a way of cross-validating the Aquarius backscatter over the ocean and found agreement to better than 1 dB for all beams. Finally we find the estimated standard deviation of the Aquarius wind speed is about 0.95 m/s, slightly worse than RapidScat.

## ACKNOWLEDGMENT

This research was carried out at the Jet Propulsion Laboratory, California Institute of Technology, under a contract with the National Aeronautics and Space Administration.

## REFERENCES

- [1] D. Le Vine, G. Lagerloef, F. Colomb, S. Yueh, and F. Pellerano, "Aquarius: An instrument to monitor sea surface salinity from space," *Geoscience and Remote Sensing, IEEE Transactions on*, vol. 45, no. 7, pp. 2040–2050, July 2007.
- [2] G. Lagerloef, F. R. Colomb, D. Le Vine, F. Wentz, S. Yueh, C. Ruf, J. Lilly, J. Gunn, Y. Chao, A. deCharon, G. Feldman, and C. Swift, "The Aquarius/SAC-D mission: Designed to meet the salinity remote-sensing challenge," *Oceanography*, vol. 21, no. 1, pp. 68–81, March 2008.
- [3] M. Shimada, "Long-term stability of L-band normalized radar cross section of Amazon rainforest using the JERS-1 SAR," *Canadian Journal of Remote Sensing*, vol. 31, no. 1, pp. 132–137, 2005. [Online]. Available: <http://pubs.casi.ca/doi/abs/10.5589/m04-058>
- [4] M. Shimada, O. Isoguchi, T. Tadono, and K. Isono, "PALSAR radiometric and geometric calibration," *Geoscience and Remote Sensing, IEEE Transactions on*, vol. 47, no. 12, pp. 3915–3932, December 2009.
- [5] S. Durden, J. van Zyl, and H. Zebker, "Modeling and observation of the radar polarization signature of forested areas," *Geoscience and Remote Sensing, IEEE Transactions on*, vol. 27, no. 3, pp. 290–301, May 1989.
- [6] O. Isoguchi and M. Shimada, "An L-band ocean geophysical model function derived from PALSAR," *Geoscience and Remote Sensing, IEEE Transactions on*, vol. 47, no. 7, pp. 1925–1936, July 2009.
- [7] A. Fore, S. Yueh, W. Tang, A. Hayashi, and G. Lagerloef, "Aquarius wind speed products: Algorithms and validation," *Geoscience and Remote Sensing, IEEE Transactions on*, vol. 52, no. 5, pp. 2920–2927, May 2014.
- [8] L. Ricciardulli and F. Wentz. (2011, April) Reprocessed QuikSCAT (V04) wind vectors with Ku-2011 geophysical model function. Remote Sensing Systems. [Online]. Available: [http://www.ssmi.com/qscat/qscat\\_Ku2011\\_tech\\_report.pdf](http://www.ssmi.com/qscat/qscat_Ku2011_tech_report.pdf)
- [9] A. Fore, B. Stiles, A. Chau, B. Williams, R. Dunbar, and E. Rodríguez, "Point-wise wind retrieval and ambiguity removal improvements for the QuikSCAT climatological data set," *Geoscience and Remote Sensing, IEEE Transactions on*, vol. 52, no. 1, pp. 51–59, January 2014.
- [10] F. J. Wentz, "A well-calibrated ocean algorithm for Special Sensor Microwave / Imager," *J. Geophys. Res.*, vol. 102, no. C4, pp. 8703–8718, 1997. [Online]. Available: <http://dx.doi.org/10.1029/96JC01751>
- [11] S. Yueh, S. Dinardo, A. Fore, and F. Li, "Passive and active L-band microwave observations and modeling of ocean surface winds," *Geoscience and Remote Sensing, IEEE Transactions on*, vol. 48, no. 8, pp. 3087–3100, August 2010.
- [12] S. Yueh, W. Tang, A. Fore, G. Neumann, A. Hayashi, A. Freedman, J. Chaubell, and G. Lagerloef, "L-band passive and active microwave geophysical model functions of ocean surface winds and applications to Aquarius retrieval," *Geoscience and Remote Sensing, IEEE Transactions on*, vol. 51, no. 9, pp. 4619–4632, September 2013.
- [13] A. Stoffelen, "Toward the true near-surface wind speed: Error modeling and calibration using triple collocation," *Journal of Geophysical Research-Oceans*, vol. 103, no. C4, pp. 7755–7766, April 1998.
- [14] J. Vogelzang, A. Stoffelen, A. Verhoef, and J. Figa-Saldaña, "On the quality of high-resolution scatterometer winds," *J. Geophys. Res.*, vol. 116, no. C10, October 2011. [Online]. Available: <http://dx.doi.org/10.1029/2010JC006640>